SOFT ROBOTICS
Volume 5, Number 1, 2018

DOI: 10.1089/soro.2016.0079

SoRo
Soft Robotics

ORIGINAL ARTICLE

Fiber-Reinforced Origamic Robotic Actuator

Juan Yi,[1,2] Xiaojiao Chen,[1] Chaoyang Song,[3] and Zheng Wang[1,2]

Abstract

A novel pneumatic soft linear actuator Fiber-reinforced Origamic Robotic Actuator (FORA) is proposed with significant improvements on the popular McKibben-type actuators, offering nearly doubled motion range, substantially improved force profile, and significantly lower actuation pressure. The desirable feature set is made possible by a novel soft origamic chamber that expands radially while contracts axially when pressurized. Combining this new origamic chamber with a reinforcing fiber mesh, FORA generates very high traction force (over 150N) and very large contractile motion (over 50%) at very low input pressure (100 kPa). We developed quasi-static analytical models both to characterize the motion and forces and as guidelines for actuator design. Fabrication of FORA mostly involves consumer-grade three-dimensional (3D) printing. We provide a detailed list of materials and dimensions. Fabricated FORAs were tested on a dedicated platform against commercially available pneumatic artificial muscles from Shadow and Festo to showcase its superior performances and validate the analytical models with very good agreements. Finally, a robotic joint was developed driven by two antagonistic FORAs, to showcase the benefits of the performance improvements. With its simple structure, fully characterized mechanism, easy fabrication procedure, and highly desirable performance, FORA could be easily customized to application requirements and fabricated by anyone with access to a 3D printer. This will pave the way to the wider adaptation and application of soft robotic systems.

Keywords: soft actuator, origami, actuator modeling, soft robots

Introduction

Soft robotics is a quickly emerging research field very promising for the emerging wearable, service, and biomimetic robot applications,[1–4] where robots physically interact with uncertain objects, unstructured environments, or humans. Such applications emphasize substantially on robot compliance and safety, together with low system complexity and cost. This feature list led to investigations on novel soft robotic actuators fundamentally distinctive from the electric motors widely adopted today, achieving inherent compliance and safety compared with the behavioral level compliance with rigid robot bodies.[5,6] The compliance of soft actuators is achieved with their flexible materials, structures, and actuation methods, for instance, flexible polymers with hydraulic or pneumatic actuation,[7–11] shape memory alloys,[12] and electroactive polymers.[13,14] In particular, flexible polymer-based fluidic actuators with the combination of high power-weight ratio, large range of motion, fast response time, and low cost. They could also achieve multiple types of motion, from contraction, extension, bending, to twisting.[7–11,15]

The McKibben actuator, aka pneumatic artificial muscle (PAM), is one of the most studied soft actuators to date.[16–21] Commercially available PAMs have been widely adopted in various industrial and academic applications.[22,23] A typical PAM design comprises of an elastomeric inner chamber inflatable by compressed air and an outer fiber-reinforced structure that converts the radial inflation into the desired axial contraction. With this simple structure and unique working mechanism, PAMs are considerably lighter and more compliant than conventional pneumatic cylinders.[24] Besides, PAMs have extremely high power to weight ratio, compact size, inherent compliance, and safety, as well as low fabrication cost. However, the elastomeric material and its characteristic working mechanism also restrict PAM's performances: the maximum theoretical contraction ratio is limited to 35%[18];

[1]Department of Mechanical Engineering, The University of Hong Kong, Hong Kong, China.
[2]HKU Shenzhen Institute of Research and Innovation (HKU-SIRI), Shenzhen, China.
[3]Department of Mechanical and Aerospace Engineering, Monash University, Clayton, Victoria, Australia.

high input air pressure is required by the actuator due to energy loss in material stretch.[17–19] There are PAM-variations trying to release this constraint; for instance, a pleated design was proposed with more than 40% maximum contraction, with significant diameter increase of more than 300%.[25] Recent studies on origamic extending soft actuators found that origamic structures could be easily actuated and substantially decrease the pressure input for desired shapes,[26,27] by rearranging and bending the origamic edges to generate motion, avoiding the internal material stretches for PAMs.

In this work, a novel Fiber-reinforced Origamic Robotic Actuator (FORA) is proposed, offering significantly improved performance over PAMs (Fig. 1). A FORA generates linear axial contractile motion when actuated by compressed air. Using an origamic inner chamber, a FORA could achieve 50% of maximum contraction, at an input pressure as low as 100 kPa. The three-dimensional (3D) printable origamic chamber could be customized with high repeatability and precision, enabling a new design dimension of inner origamic chamber toward the desired actuator performance specifications.

This article is organized as follows: static models of the FORA revealing relations among traction force, pressure, and contraction ratio are presented in Actuator Concept and Modeling section; Actuator Design section presents the actuator design and fabrication; experimental validations are presented in Evaluation Experiments and Results section; finally in Antagonistic Robotic Joint section, an antagonistic robotic joint driven by two FORAs is presented to showcase the clear benefits brought by the superior FORA performances.

Actuator Concept and Modeling

The proposed FORA design as shown in Figure 1 has an internal inflatable chamber and an external layer of reinforcing fibers similar to a typical PAM design. However, their mechanisms of motion and force generation are substantially different. To expatiate these distinctions, existing models of the PAM are briefly reviewed, before proposing the concept and models of the new FORA design.

Modeling of PAM

The inflatable inner chamber of a PAM deforms during actuation, resulting in a finite range of motion and a correlating output force. Existing static models of PAMs capture the relations among the relative pressure P, the output traction force F, and the actuator contraction ratio or fiber braiding angle θ, usually developed from two approaches[17]: energy conservation[18] and surface pressure equilibrium.[19,20] Both approaches resulted similarly that the static PAM model is as follows[18]:

$$F = \frac{Pb^2\left(2\cos^2\theta - \sin^2\theta\right)}{4\pi n^2}, \tag{1}$$

where the traction force F is presented as a monotonic function of braiding angle θ. b is the total length of one fiber, n is the number of cycles that one fiber turns around the whole body of inner chamber.

To further explain the components of F and investigate the maximum contraction of McKibben-type actuators, deriving from the model of Equation (1), the traction force F could be rewritten as

$$F = F_{body} - F_{end} = \frac{2Pb^2\cos^2\theta}{4\pi n^2} - \frac{P\pi D^2}{4}, \tag{2}$$

where F_{body} is the body contraction force due to radial expansion which is related to the mesh dimensions, and F_{end} is the end extension force due to internal pressure acting on the air chamber ends. $D = b\sin\theta/(n\pi)$ is the diameter of PAM. The end extension force

$$F_{end} = P\pi D^2/4, \tag{3}$$

is an important limiting factor for the performance of PAM. For instance, for a PAM with initial diameter$D_0 = 40mm$, the end force rises to 125N under 100 kPa input pressure based on the calculation of Equation (3) and increases as the actuator contracts (D increases). Following Equation (2), the end force will eventually balance the body force, that is, $F = 0$, at $\theta = 54.7°$, limiting the maximum contraction of PAMs to around 35%, while substantially reducing the traction force. If the energy consumptions of materials stretch and friction are also taken into consideration, maximum PAM contraction will be limited further to 20–30%.[17,19,20]

FIG. 1. Concept of FORA. *Upper*: pressurized state, *lower*: natural state. The design consists of an inner origamic chamber, an external braided mesh, and connection fittings. FORA, Fiber-reinforced Origamic Robotic Actuator.

Concept of FORA

The novel FORA concept aims to increase the motion range and improve the output force profile over PAMs, by eliminating the end extension force and reducing the material stretch of inner chamber. To achieve this, the FORA concept mainly comprises an inner origamic chamber and an outer fiber-braided mesh. The origamic chamber of FORA is the main novelty and key distinction. Exploiting special origamic patterns, the chamber will expand radially while contract axially when pressurized. The radial expansion will then change the fiber braiding angle and generate contractile motion, as well as traction force. Hence, the fiber braiding angle is a variable directly correlated to the contractile motion of FORA. This relation will be explored in the following.

A FORA has two mirroring halves, each has two geometrical sections (Section 1 and Section 2 in Fig. 2(b)). The overall actuator length L is:

$$L = 2(l_1 + l_2), \tag{4}$$

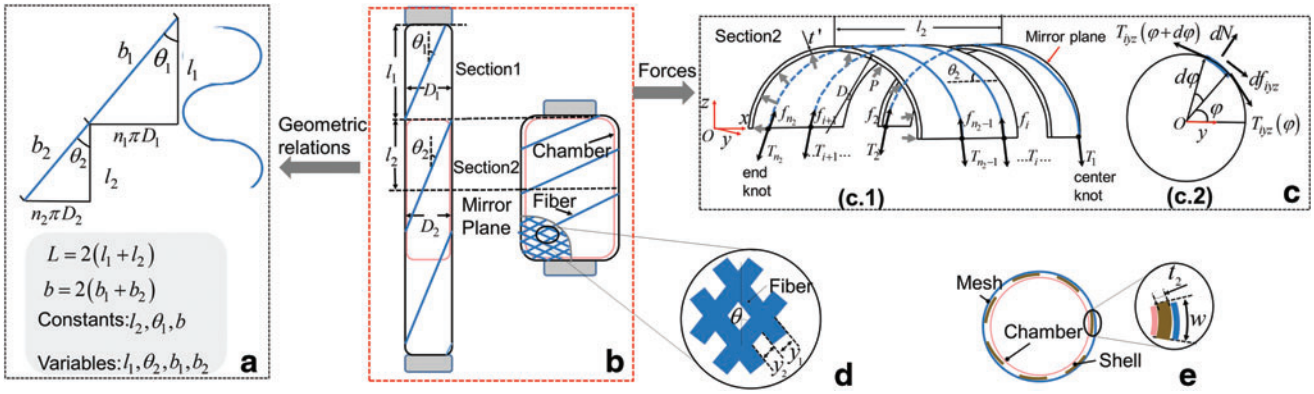

FIG. 2. Schematic drawings of the FORA concept, where the actuator is divided into two symmetric halves along the mirror plane, each with two sections. **(b)** FORA in pressurized state (*right*) and natural state (*left*). The components of FORA are indicated in the figure. **(a)** A segment of the fiber winding in the winding (*right*) and straighten (*left*) states. Geometric relations of the FORA are illustrated. **(c)** Schematic model of forces in Section 2: (c.1) Force diagram of Section 2 with one fiber turning around. Section 2 was cut by x–y Plane and Mirror Plane. (c.2) Force diagram of an infinitesimal fiber element decomposed to the cross section. **(d)** One cell of the braiding mesh. **(e)** Cross section of FORA with shells pasted to the chamber. Color images are available online at www.liebertpub.com/soro

where l_1, l_2 are the lengths of Section 1 and Section 2, respectively. Assuming fibers turn around a perfect cylinder, for the braided pattern of mesh as shown in Figure 2(a), the geometrical dimensions of Section 1 and Section 2 satisfy

$$\begin{cases} l_1 = b_1 \cos\theta_1 = n_1 D_1 \pi \cot\theta_1 \\ l_2 = b_2 \cos\theta_2 = n_2 D_2 \pi \cot\theta_2, \\ b = 2(b_1 + b_2) \end{cases} \tag{5}$$

where b_1, b_2 are the lengths of the fiber's segment turning around Section 1 and Section 2, D_1, D_2 are the diameters of two sections, respectively. n_1, n_2 are the number of cycles that one fiber wind in Section 1 and Section 2. When FORA is actuated, braiding angle of Section 1 θ_1 is a constant, while braiding angle of Section 2 θ_2 increases. Substituting Equation (5) into Equation (4),

$$L = b\cos\theta_1 + 2l_2(\cos\theta_2 - \cos\theta_1)/\cos\theta_2, \tag{6}$$

where L decreases monotonically as θ_2 increases.

$$\theta_2 = \arccos\left(\frac{2l_2\cos\theta_1}{b\cos\theta_1 - L + 2l_2}\right). \tag{7}$$

Defining a contraction ratio x as

$$x = (L_0 - L)/L_0, \tag{8}$$

where L_0 is the initial length of FORA. When x reaches to its maximum contraction ratio $x_{\max}$, the two ends of FORA will coincide with the ends of the chamber, such that

$$x_{\max} = (L_0 - 2l_2)/L_0. \tag{9}$$

Deriving from Equation (8),

$$L = L_0 - L_0 x. \tag{10}$$

By substituting Equation (10) into Equation (7), θ_2 can be determined by the contraction ratio x,

$$\theta_2 = \arccos\left(\frac{2l_2\cos\theta_1}{b\cos\theta_1 - (L_0 - L_0 x) + 2l_2}\right). \tag{11}$$

The relationship between θ_2 and dimensional constants, l_2, L_0, and θ_1, together with contraction ratio x is illustrated in Equation (11). The contraction ratio is shown to be the unique variable dictating the fiber braiding angle θ_2.

Modeling of FORA

In this section, a static model of FORA is formulated to capture the relations among pressure, braiding angle, and traction force.

The fundamental component we considered is the fiber as it is the key to convert input pressure into contractile motion and traction force. The supplied air pressure applies on the origamic chamber, gets transmitted to the fiber, therefore generating traction force. As mentioned, one of the improvements of the origamic chamber, comparing to the conventional elastomeric inner chamber,[17] is that it reduces the energy input to stretch material by rearranging the chamber structure, therefore keeping the stored energy to a minimal level. Therefore, we ignore this energy in our model considering the unique design of origamic chamber. Forces balanced with applied air pressure of P in z direction[17,20] (Fig. 2(c.1)) could be obtained as

$$Pl_2(D_2 - 2t_1) = 2\sin\theta_2\left(\sum_{i=2}^{n_2}(T_i + f_i) + T_1\right), \tag{12}$$

where t_1 is the chamber thickness, i is the number of fiber knots in plane x–y, which are labeled from the center to the end of Section 2 with total n_2 knots. We define the tension force of fiber and friction resulting from interactions between the fiber and the origamic chamber on the i_{th} knot as T_i and f_i. In this study, the fiber is assumed to be inextensible. The Coulomb friction model is adopted in this work to calculate f_i, since it is generally accepted as the dominating frictional force in previous studies on fiber-reinforced actuators.[17,18,20]

Relations of frictional force and tension force in the center knot to the end knot could be presented as

$$T_1 = T_2 + \lambda f_2 = \ldots\ldots = T_i + \lambda f_i = \ldots\ldots = T_{n_2} + \lambda f_{n_2}. \quad (13)$$

λ indicates the direction of friction relating to the motion direction of fiber.

$$\begin{cases} \lambda = -1, v_x < 0 \\ \lambda = 1, v_x \geq 0 \end{cases},$$

where $v_x < 0$ means the actuator contracting, $v_x \geq 0$ means the actuator extending.

Substituting Equation (13) into Equation (12),

$$Pl_2(D_2 - 2t_1) = 2n_2 T_1 \sin\theta_2. \quad (14)$$

The output traction force F (in x direction) could be presented as

$$F = T_{n_2} \cos\theta_2. \quad (15)$$

To obtain the traction force in Equation (15), according to the relations of T_1 and T_{n_2} in Equations (13) and (14), frictional force f_i needs to be obtained from the analysis on the cross-sectional surface, Plane y–z, as in Figure 2(c.2). Regarding an infinitesimal fiber element,

$$\begin{cases} T_{iyz}(\varphi + d\varphi) - T_{iyz}(\varphi) = df_{iyz} \\ T_{iyz} d\varphi = dN \\ df_{iyz} = \mu \sin\theta_2 dN \end{cases}, \quad (16)$$

where T_{iyz} is the tension force of one fiber decomposed into the Plane y–z,

$$T_{iyz} = T_i \sin\theta_2, \quad (17)$$

φ is the central angle of the arc as in Figure 2(c.2), N is the force acting on the fiber perpendicularly, f_{iyz} is the frictional force of fiber in the cross section, and μ is the frictional coefficient. The value of μ mainly depends on the contact conditions of braiding mesh. The braid comprises of quadrangle cells, as illustrated in Figure 4(d). Each cell consists of four crossover points. Two types of contact occur in each cell: one type is the fiber segment in contact with another fiber in the crossed points; the other one is the fiber segment directly in contact with the chamber. We define that the frictional coefficient between fiber and fiber is μ_1, frictional coefficient between fiber and chamber is μ_2. Then, in one braid cell,

$$\mu = \frac{y_1}{y_1 + y_2}\mu_1 + \frac{y_2}{y_1 + y_2}\mu_2, \quad (18)$$

where y_1, y_2 is the length of fiber in contact with other fibers and the chamber, respectively. In this study, each cell in the mesh has dimensions $y_1 = y_2$. Therefore,

$$\mu = (\mu_1 + \mu_2)/2. \quad (19)$$

Based on Equations (16), (17), and (19), relationships between T_1 and T_{n_2} could be derived as

$$T_{n_2} = T_1 e^{-n_2(\mu_1 + \mu_2)\pi \sin\theta_2}. \quad (20)$$

Consequently, by substituting Equation (20) into Equations (14) and (15),

$$F = Pl_2(D_2 - 2t_1)e^{-\lambda n_2(\mu_1 + \mu_2)\pi \sin\theta_2}\cos\theta_2/(2n_2 \sin\theta_2). \quad (21)$$

Substituting Equation (5) into Equation (21),

$$F = \frac{1}{2}P(D_2 - 2t_1)^2 e^{-\lambda n_2(\mu_1 + \mu_2)\pi \sin\theta_2}\cot^2\theta_2, \quad (22)$$

where the parameter $e^{-n_2(\mu_1 + \mu_2)\pi \sin\theta_2}$ is from the Coulomb friction, correlating to the fiber braiding angle θ_2, the winding numbers of fiber n_2, and the frictional coefficients μ_1, μ_2. To reduce the friction between the inner chamber and mesh, we took measures to reduce μ_2 and contact area by attaching rigid polytetrafluoroethylene (PTFE)-coated shells with thickness of t_2 to the surface of chamber (Fig. 2(e)). As a result, parameters $h = 4w/\pi D_2$ and t_2 should be considered in Equation (14) which should be rewritten as

$$hPl_2(D_2 - 2t)^2 = 2n_2 T_1 \sin\theta_2, \quad (23)$$

where $t = t_1 + t_2$. Hence, the static model could be represented as follows:

$$F = hP(D_2 - 2t)^2 e^{-\lambda h n_2(\mu_1 + \mu_2)\pi \sin\theta_2}\cot^2\theta_2/2. \quad (24)$$

This static model of Equation (24) reveals the correlations of traction force, pressure, and braiding angle. The traction force is proportional to the pressure and also monotonically decreases as the braiding angle increases. In the following study, Equation (24) will be further used to guide the FORA's design for its desirable characteristics. Experimental validations of Equation (24) will be conducted in Evaluation Experiments and Results section.

Actuator Design

Following the discussion of concept, this section presents the design details and selection of materials of three components: the inner origamic chamber, the fiber-braiding mesh, and connection fittings.

Origamic chamber design

The novel features of the FORA design are mainly achieved by the novel origamic chamber. As mentioned in the Actuator Concept and Modeling section, two features of the chamber are required:

1. Design of the chamber takes advantage of the origamic pattern generating the motion by structure rearrangement instead of material stretch.
2. Motion of the chamber follows expansion radially to generate desired actuator motion and force, while the axial extension is constrained to eliminate the end extension force.

To achieve this unique feature set, we take inspirations from three basic folding patterns: the water-bomb (WB) pattern,[27]

the tree-leaves (TL) pattern,[28] and the Miura-ori (MO) pattern[29] in designing the origamic chamber in this study. As shown in Figure 3(a), the basic frame of the origamic chamber is WB, which unfolds to an enclosed chamber by taking advantage of the foldability of end caps in 3D space. Further improvements on the basic structure are made: the TL pattern can further fold the end cap into a smaller structure; the MO pattern is used to transform from the end cap to the body. The effective length of body in contact with the outer mesh is a constant of $2l_2$ during actuation.

The radial deformation of the origamic chamber is investigated, as the radial expansion correlates to the diameter of the FORA and further affects the traction force as modeled in Equation (24). To quantify it, we define the radial deployable ratio k_1 of the end cap, as in Figure 3(b) (view in direction of the red arrow of Fig. 3(a)).

$$k_1 = R_{\max}/R_{\min}, \tag{25}$$

where the end cap is approximated to a circle with radius of R. $R_{\max}$ and $R_{\min}$ are the radiuses of the fully deployed end cap and fully folded end cap, respectively. The end cap is characterized by parameters c_0, c_1, c_2, c_3, c_4, which should follow these relations.

$$\begin{cases} c_0 = \sum_{i=1}^{4} c_i \\ c_{i-1, i=1,2,3,4} \geq c_{i, i=1,2,3,4} \end{cases}. \tag{26}$$

$R_{\max} = \sqrt{c_0^2 + (c_0 c_4)^2}$ as indicated in Figure 3(b) (left). $R_{\min} = c_1$ when the chamber is fully folded. Therefore,

$$k_1 = \sqrt{c_0^2 + (c_0 c_4)^2}/c_1. \tag{27}$$

End caps with increased numbers of ridges N are listed in Figure 3(b). These end caps share the same equation to calculate the radial deployable ratio Equation (27). If we substitute Equation (26) into Equation (27),

$$k_1 \leq 5. \tag{28}$$

Maximum deployable ratio of 5 is achieved when $c_1 = c_2 = c_3 = c_4$. This maximum deployable ratio is large enough to suit the radial inflation ratio of outer mesh according to the following studies on the outer mesh. An end cap with more ridges could better approximate a circle, making the chamber closer to a cylindrical shape. However, ridges where walls intersect will decrease the value of k_1 because of the effects of wall thickness. To achieve both the greater approximation to the circle and less effects to the deployable ratio, $N = 4$ has been chosen in this design.

Fiber mesh and connection fittings

In the design of FORA, $k_1 \leq k_2$ should be satisfied to achieve good performance. k_2 is defined as the radial expansion ratio of the outer mesh and could be presented as

$$k_2 = D_{\max}/D_{\min}. \tag{29}$$

where $D_{\max}$, $D_{\min}$ are the maximum and minimum diameters of the mesh. According to the geometric relations of the actuator, Equation (29) could be presented as a function of braiding angle

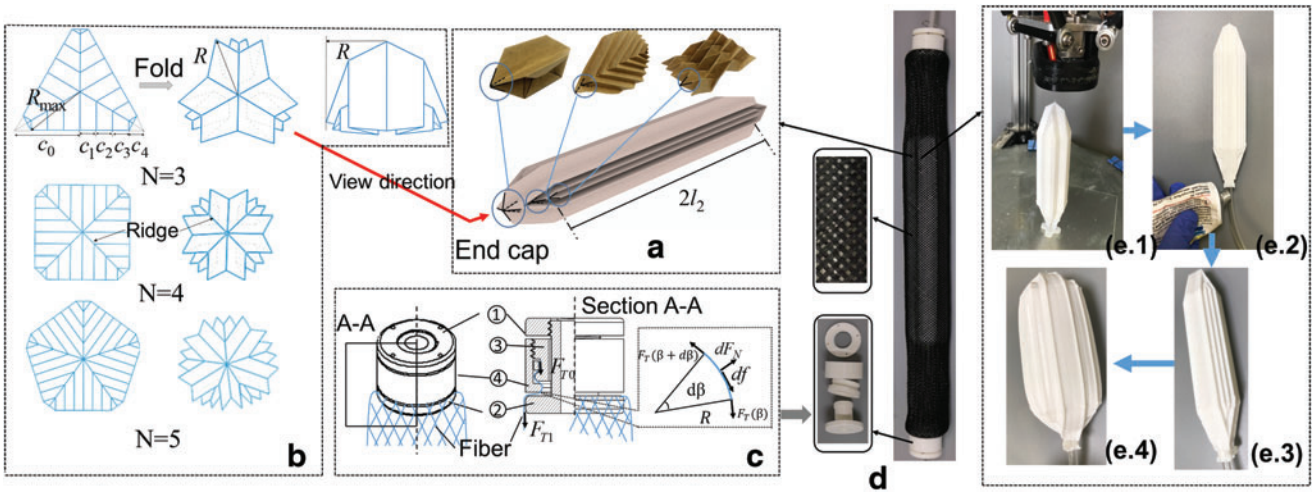

FIG. 3. Design and fabrication of FORA. **(a)** Concept of the origamic chamber with basic origami patterns (WB pattern, TL pattern, and MO pattern). The units adopted from these basic patterns are depicted with *black lines* in the *circles*. **(b)** Schematic of End caps of origamic chamber (view in direction of the *arrow* in **[a]**) with different number of ridges, *left*: fully deployed, *right*: half folded. **(c)** Schematic design of the connection fittings. *Left*: overview of connection fittings; *right*: schematics. **(d)** A fabricated prototype of FORA, consisting of an internal origamic chamber, an external mesh, and connection fittings. **(e)** Fabrication process of the origamic chamber: (e.1) Print the origamic chamber; (e.2) Insert the pneumatic tube to the chamber and use glue to seal the connection; (e.3) The origamic chamber in natural state; (e.4) The origamic chamber in expansion state. The process from the natural state to the expansion state is shown in Supplementary Video S1 (Supplementary Data are available online at www.liebertpub.com/soro). MO, Miura-ori; TL, tree-leaves; WB, water-bomb. Color images are available online at www.liebertpub.com/soro

$$k_2 = \sin\theta_{\max}/\sin\theta_{\min}, \quad (30)$$

where $\theta_{\max}$, $\theta_{\min}$ are the maximum and minimum braiding angles of the mesh, both measured by a protractor.

The connection fittings hold both ends of the fiber mesh and transmit the traction force to external payload. Therefore, the connection fittings should be easy to reassemble and have high tensile strength. The design of the connection fittings consists of four components as illustrated in Figure 3(c). The center of the cylindrical body is hollow for the pneumatic tube to connect to the inner chamber. Component ① provides anchor points at its top plate to mount the actuator externally. Components ②, ③, and ④ are used to clamp the braided fibers by utilizing thread and screw.

To avoid stress concentration, convexities and fillets at all corners are used. A segment of fiber with central angle β is shown in Figure 3(c), with forces in radial and tangential directions satisfy the following relations:

$$df + F_T(\beta) = F_T(\beta + d\beta), dF_N = F_T d\beta, df = \mu_3 dF_N, \quad (31)$$

where df is the frictional force acting on the element, F_T is the tension force along the fiber, dF_N is the force perpendicular to the fiber, and μ_3 is the static friction coefficient between the fiber and clamp parts. Therefore, tension forces of the fiber are reduced from F_{T_1} to F_{T_0} by the components ②, ③, and ④

$$F_{T_1} = F_{T_0} e^{-5\pi\mu_3}. \quad (32)$$

For the connection fitting design in this study, tension forces of the fiber are significantly reduced by over 20 times benefiting from the mechanical design, which significantly lower the requirements on the material strength. As a result, with polylactide (PLA) printing material, the proposed connection fittings could be utilized in the FORA to provide high tensile strength for holding the outer mesh.

Materials and dimensions

When selecting materials for the FORA design, it is essential that all components could sufficiently withstand both the input air pressure and the resulting traction force. In contrast, with the fast development of 3D printing technology, it is desirable for the FORA construction to use 3D-printed parts as much as possible for fast design iteration and maximum customizability at low cost. With carefully chosen structure wall thickness and printing parameters, the 3D-printed chamber could achieve very good airtightness, sufficient in withstanding the target air pressure in this application. The fabrication process is demonstrated in Figure 3(e). Five origamic chambers showing the actuation process are demonstrated in the Supplementary Video S1 (Supplementary Data are available online at www.liebertpub.com/soro). The printing material is flexible thermoplastic polyurethane (NinjaFlex®, Shore Hardness: 85A). Moreover, with the design considerations in reducing stress concentration, as discussed, the connection fittings could be fabricated with 3D-printed PLA material. Nylon is used for the braided fiber mesh, due to its relatively high tensile strength. Frictional coefficients of these materials are listed in Table 1.[30,31]

The FORA design offers a high degree of customizability. Both the initial and actuated length/diameter of FORA could be customized according to the stroke and force requirements. In this study, an initial diameter of 30 mm was chosen for FORA, similar with commercially available PAMs for comparability. Subsequently, the initial diameter was 25 mm for the origamic chamber to fit the outer mesh. The initial length of FORA is 260 mm to fit both the 3D-printer volume and the testing platform dimensions for evaluation. Effective length of origamic chamber ($2l_2$) is set to be 120 mm to achieve more than 50% maximum contraction ratio regarding the calculation of Equation (9). The prototype of FORA is shown in Figure 3(d).

Table 1. Materials Properties

Component name	*Material*	*Frictional coefficients (with nylon)*
Fiber-braided mesh	Nylon	0.15–0.25
Origami chamber	Flexible TPU	NA
Connection fittings	Hard PLA	0.25
Chamber shells	Hard PLA (lubricant with PTFE)	0.16

NA, not applicable; PLA, polylactide; PTFE, polytetrafluoroethylene; TPU, thermoplastic polyurethane.

Evaluation Experiments and Results

Experiment platform

Soft actuators follow fundamentally different working principles from traditional robotic actuators. We developed a dedicated soft actuator evaluation platform with regulated pneumatic supply, 2 Degree-of-Freedom (DOF) motorized position measurement and control, real-time display of measurements, and recording functions. The platform consists of two sliding rails (X- and Y-sliders) in the horizontal and vertical directions independently driven by motors (NEMA 57 stepper motors, 200 steps per revolution), a load cell (±500N max.) fixed on either slider to obtain the axial pulling force of linear actuators, a digital camera for recording the motion of the target, and a series of pneumatic components: a computer-controlled pressure regulator (SMC, ITV1030, 500 kPa max.) equipped with an air filter and a manual pressure regulator for air preprocessing, pressure sensors (Honeywell 500 kPa max.), and pneumatic micro valves (SMC, SY113A-5LZ-PM3-F, 700 kPa max.). A photo of the platform is shown in Figure 4(a). The user interface of the platform was developed using NI LabVIEW 2013. The experiment platform is capable of real-time displaying and recording of pressure, force, and motion feedbacks by the pressure sensor, axial sensor, and camera, respectively. The experiment platform facilitates linear or bending soft actuators with motion range up to 400 mm horizontally and 200 mm vertically under different actuation and loading conditions.

To validate the relations among pressure, contraction ratio, and traction force, quasi-static experiments were conducted under free space, isometric, and isotonic conditions, where the actuators were assumed to move sufficiently slow to ignore any dynamics. In the remainder of this section, we will present quasi-static experimental results of FORAs conducted on the experiment platform, in comparison with the simulation results from the static model and experimental

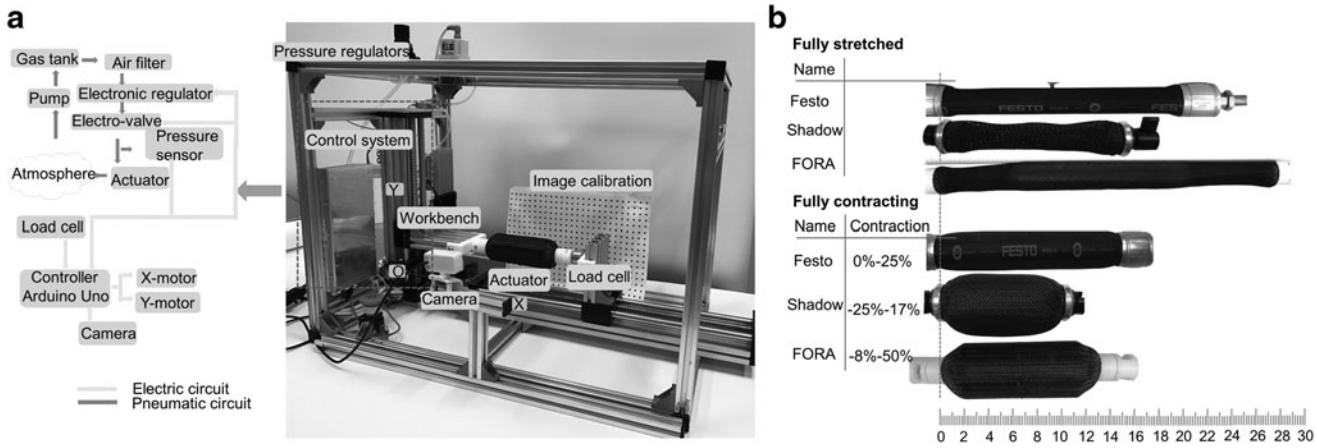

FIG. 4. **(a)** Experiment platform. Test samples are mounted on the workbench. **(b)** Three types of actuators (Festo, Shadow, and FORA) in two states (fully stretched and contracting). In the fully stretched state (*upper*), both FORA and Shadow are stretched with external load. Festo is in free space. In the fully contracting state (*lower*), Festo, Shadow, and FORA are contracting in free space.

measurements from commercially available PAMs. Two of the most popular PAMs were chosen: the Air Muscle from Shadow Robotics (Shadow, S30AM-S-1) and the Fluidic Muscle from Festo (Festo, DMSP-20-200N). The dimensions of the three actuators were as follows: FORA: $L_0 = 260mm$, $D_0 = 30mm$, Shadow: $L_0 = 120mm$, $D_0 = 30mm$, and Festo: $L_0 = 200mm$, $D_0 = 20mm$. Three comparable actuators are shown in Figure 4(b), where both FORA and Shadow show negative contraction ratio when loaded. The angles of outer mesh could be further reduced based on the unique structures and materials of inner chamber with the assistance of external force. This negative contraction ratio effectively extended the range of contraction ratio. Full range of contraction ratio (negative and positive contraction) of FORA is well illustrated: in free space (no external load), FORA reached its maximum contraction (50%) at the input pressure of 100 kPa. Shadow reached its maximum contraction (17%) at the input pressure of 200 kPa. Twenty-five percent of contraction ratio of Festo was achieved with the higher input pressure around 400 kPa.

Free space test

In free space experiments, there was no external load, hence the traction force was zero, and only the pressure-to-contraction relation was validated. The pressure was increased by 1 kPa/s, the resulting contractile displacements were followed by the X-slider with a resolution of 0.5 mm while keeping zero traction force. The actuators were mounted on the workbench, with one end fixed to the load cell on the X-slider to read the traction force. Two FORAs with identical dimensions together with Shadow and Festo actuators were tested, each repeated thrice for repeatability validation.

Figure 5(a) shows the contraction ratios of FORAs, Shadow, and Festo against pressure. For Shadow and Festo actuators, due to nonlinear inner-chamber elasticity, small displacement occurred until the pressure reached to 50 and 100 kPa, while the threshold pressure was as low as 5 kPa for FORA. At 100 kPa, FORA had already reached the maximum contraction ratio of 50%, doubling the contraction ratio of PAMs (20–30%). After we increased the pressure to 200 kPa, the Shadow and Festo both achieved larger contraction of 10% and 11%.

FORAs significant improvements over PAMs were mainly due to two reasons: (1) the unique origamic chamber design eliminated force loss at two ends and (2) the origamic chamber also minimized the input pressure to chamber deformation. A significant by-product is the substantially reduced input pressure of 100 kPa. In addition, the highly agreeing results of two FORAs demonstrated the high repeatability of both the FORA design and the 3D-printing-based fabrication process.

Isometric test

The force–pressure relation was investigated in isometric tests. In an isometric condition, one end of the actuator was fixed to the workbench on the platform and the other end to the X-slider with a fixed position. Traction forces were measured at different input pressure for the particular contraction ratio.

Results on traction force-pressure relations at contraction ratios of −3.85%, 0%, and 3.85% are plotted in Figure 5(b). Experimental results demonstrated a very good linearity between the traction force and the input pressure, in good agreement with the static model of FORA Equation (24), with slight deviations due to the unmodeled nonlinearities in the actuator. These deviations were most significant between 0 and 10 kPa, suggesting an unmodeled initial pressure to deploy the origamic chamber, which quickly became negligible at higher pressure values.

Isotonic test

In the isotonic condition, a constant air pressure was supplied to the actuator. The traction force was changed with contraction of actuator: (1) Test started from the maximum extension position of −7%; (2) One end of actuator connected to the X-slider was pulled at 15 mm increments until the actuator reached maximum contraction; and (3) The procedure was reversed from maximum contraction to the maximum extension. Traction forces and contraction ratios were recorded in this test. The results exhibited the traction forces in FORA contracting and extending. Experiments were performed at pressures of 50 and 100 kPa, respectively.

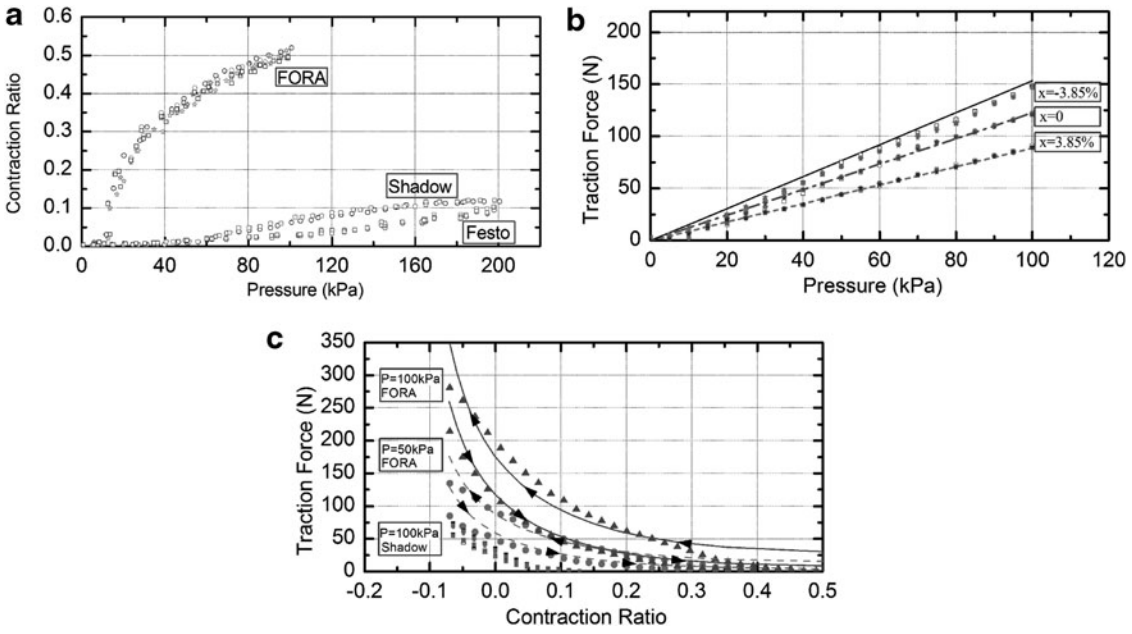

FIG. 5. Experimental results, symbols: experimental results, each group of symbols means one repeating test results. *Lines*: modeling results. **(a)** Free space test, results on FORA, Shadow, and Festo are compared. **(b)** Isometric test. **(c)** Isotonic test. The *arrows* describe the motion directions of FORA.

The experiment results are shown in Figure 5(c). At a constant pressure, maximum traction force was achieved at minimum contraction (or maximum extension in this case). With the increase of contraction ratio, traction force decreased and eventually reached zero at maximum contraction. Modeled results Equation (24) also demonstrated this relation with slight deviations at negative contractions, likely due to unmodeled nonlinearities. The experimental results of Shadow at 100 kPa were compared with FORA results in Figure 5(c), where FORA had over five-time higher forces than Shadow at the same contraction ratios.

Antagonistic Robotic Joint

The superior performances of FORA could bring significant benefits to robotic applications. In this section, a rotational robotic joint inspired from the antagonistic human biceps–triceps system (Fig. 6(a)) was built using two FORAs configured antagonistically, showcasing the improvements from their large-range contractile motion, natural compliance, and high power-to-weight ratio.

Previous works on antagonistic joint utilizing PAMs have proven the ability and merits of antagonistic joints in performing multi-DOF motions.[20,32–34] However, the 30% motion range of PAMs limited their applications: a very long arm is required to house the PAM sufficient in producing the required deformation on the joint.[32] With the nearly-doubled motion range of FORA, we could achieve large motion with small arm length, enabling much more flexible robotic design.

Design and modeling

The antagonistic robotic joint consists of a 1-DOF rotational linkage driven antagonistically by two FORAs (FORA 1

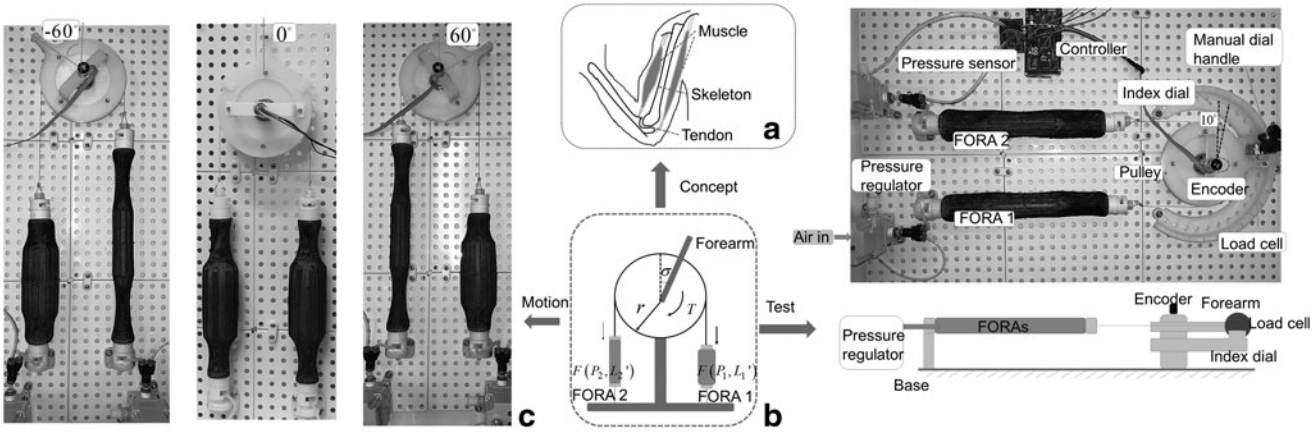

FIG. 6. Workflow of antagonistic robotic joint. **(a)** Human Biceps–triceps system. **(b)** Schematics of the antagonistic robotic joint. **(c)** Motions in $\sigma = -60^\circ$, $P_1 = 0$kPa, $P_2 = 50$kPa; $\sigma = 0^\circ$, $P_1 = 25$kPa, $P_2 = 25$kPa; and $\sigma = 60^\circ$, $P_1 = 50$kPa, $P_2 = 0$kPa. **(d)** Test panel for the antagonistic joint: photo in *top* view (*upper*) and schematic from *side* view (*lower*).

and FORA 2 in Fig. 6(b)), both connected to a pulley by cables similar to the human biceps–triceps system. Rotation starts from the initial position where FORA 1 and FORA 2 are at the same initial pressure P_0 and initial length L_0' to keep the forearm in a central position with the joint angle $\sigma = 0°$. We define $\sigma > 0°$ when the joint rotates clockwise and $\sigma < 0°$ when the joint rotates anticlockwise. From this initial position, according to the static model Equation (24), pressure differences in FORA 1 and FORA 2 will generate force differences resulting in a torque on the joint. Therefore, rotation of the antagonistic joint is generated by changing the input pressure P_1 and P_2.

A proper strategy to actuate the joint is increasing the pressure ΔP of one FORA and simultaneously decreasing the pressure of the other one:

$$\begin{cases} P_1 = P_0 + \Delta P \\ P_2 = P_0 - \Delta P \end{cases}. \tag{33}$$

Principle variables describing the characteristics of antagonistic joint are: torque T, joint angle σ, and pressures P_1, P_2, with

$$\begin{cases} T = (F_1 - F_2)r \\ \sigma = (L_1' - L_2')/-2r \end{cases}, \tag{34}$$

where L_1', L_2' denotes the length of FORA 1 and FORA 2, $L_1' = L_0' - r\sigma, L_2' = L_0' + r\sigma$, r is the radius of pulley, F_1,F_2 are the traction forces generated by FORA 1 and FORA 2, from Equation (24):

$$\begin{cases} F_1 = F(P_1, \theta_2(L_1)) \\ F_2 = F(P_2, \theta_2(L_2)) \end{cases}, \tag{35}$$

where $\theta_2(L_1)$ and $\theta_2(L_2)$ could be calculated with Equation (7).

Specifications of the antagonistic joint are listed in Table 2. Motion demonstration of the antagonistic joint in free space is shown in Figure 6(c), where the whole motion range ([−60°,60°]) is demonstrated. Comparing to the traditional PAM-built robotic joint with same dimensions (L_0, r), joint motion range is doubled benefiting from the doubled contraction ratio of FORAs.

Static characteristics

To characterize the antagonistic joint, a platform was developed to validate the relations among pressure, joint angle, and torque, as in Figure 6(d). In this platform, a manual dial handle was utilized to drive the forearm rotating in the index dial plane. And the load cell was mounted on the handle to record the driving forces and finally get the torque of the joint. The joint angle was recorded by a rotary encoder (360° max.) in real time. The index dial was designed with holes to fix the manual dial handle, as well as the forearm with a resolution of 10° joint angle. Pressures of FORA 1 and FORA 2 were controlled and recorded by two electric pressure regulators (SMC, ITV2030, 100 kPa max.).

Table 2. Specifications of Antagonistic Joint

FORA			*Antagonistic joint*		
$L_0(mm)$	x (used)	$r(mm)$	σ(deg)	Peak torque	Pressure range
260	46%	57.5	120	8 Nm	0–100 kPa

L_0, the initial length of FORA; x, the contraction ratio of FORA used in the robotic joint; r, the radius of pulley; σ, joint angle.
FORA, Fiber-reinforced Origamic Robotic Actuator.

Isometric tests were performed referring to the same states when testing FORAs, where the forearm of the antagonistic joint was fixed to the index dial in a certain angle. An initial pressure of $P_0 = 50$kPa was applied to the FORA 1 and FORA 2. We increased the pressure of FORA 1 at 10 kPa increments within the working pressure range of 0–100 kPa. In the meantime, the pressure of FORA 2 was decreased with the same amount. The $T - \Delta P$ relations in a fixed position are plotted in Figure 7, where torques at $\sigma = -60°$, $\sigma = -30°$, $\sigma = 0°$, $\sigma = 30°$, and $\sigma = 60°$ are presented. The experimental results demonstrate that the joint torques proportionally increase following the increase of ΔP. A maximum torque of 8 Nm is achieved when $\Delta P = 50$kPa in $\sigma = 60°$ in this working range, agreeing with the modeling results, and therefore verifying the static model of antagonistic joint. Slight deviations at the extreme positions are observed, similarly to the deviation of static model on FORA at its negative contractions.

Joint compliance

A unique and important feature of antagonistic joint is the variable compliance C, which is defined as

$$C = k^{-1} = \Delta\sigma/-\Delta T, \tag{36}$$

where k is the joint stiffness, $\Delta\sigma$ is the angle differences produced by the applied torque to the joint, ΔT. Compliance of the antagonistic joint describes the ability of reacting to the external load with deformation and could be variable in the antagonistic joint.

In the test platform (Fig. 6(d)), compliances of the antagonistic joint were measured by recording ΔT and $\Delta\sigma$ at constants of pressure. Tests were conducted in three steps: (1) Two FORAs were actuated under pressure of P_1, P_2. The forearm was fixed at designated angles. (2) Move the forearm

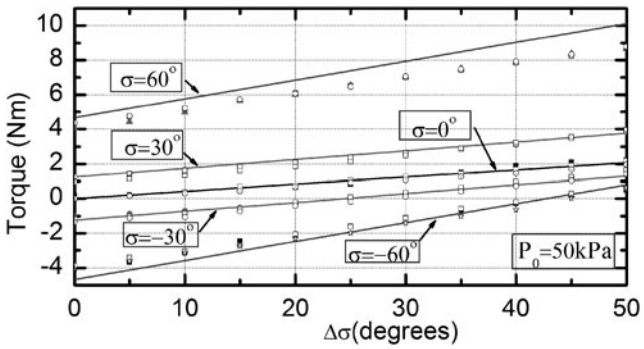

FIG. 7. Isometric results of the antagonistic joint, *dots:* experimental results, each group of symbols means one repeating test results. *Lines*: modeling results.

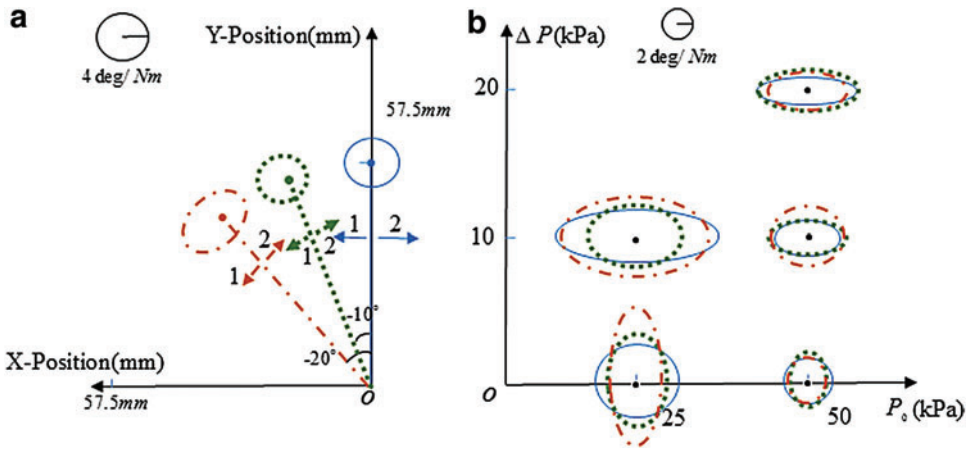

FIG. 8. Joint compliance test results. **(a)** Compliances in $\sigma = 0^\circ$ (*solid ellipse*), $\sigma = -10^\circ$ (*dotted ellipse*), $\sigma = -20^\circ$ (*dashed ellipse*), with $P_0 = 25$kPa and $\Delta P = 0$kPa. O is the joint, the center of ellipse is the position of forearm tip. The radius in directions 1 and 2 are the joint compliances in these two directions. **(b)** Compliances at a series of P_0, ΔP, and σ values. The major radius of ellipse is the measured compliance in anticlockwise direction; the minor radius of ellipse is compliance in clockwise direction. Color images are available online at www.liebertpub.com/soro

clockwise with $\Delta\sigma = 3^\circ$ and record ΔT. (3) Repeat the procedure in anticlockwise direction. The results are shown in Figure 8, with the variable compliances in different P_0, ΔP, and σ. Therefore, variable compliances could be obtained in the antagonistic robotic joint with variable input pressure P_0, ΔP.

Dynamic response

Although the main content of this article has been focused on static and quasi-static performances, in this section the dynamic response of the antagonistic joint was tested to provide a glimpse on the capabilities of FORA. In the test platform (Fig. 6(d)), the pressure regulators were capable of automatic pressure regulations with their inner control circuits. A proportional control strategy was applied to control the joint angle σ to follow a desired trajectory in free space.

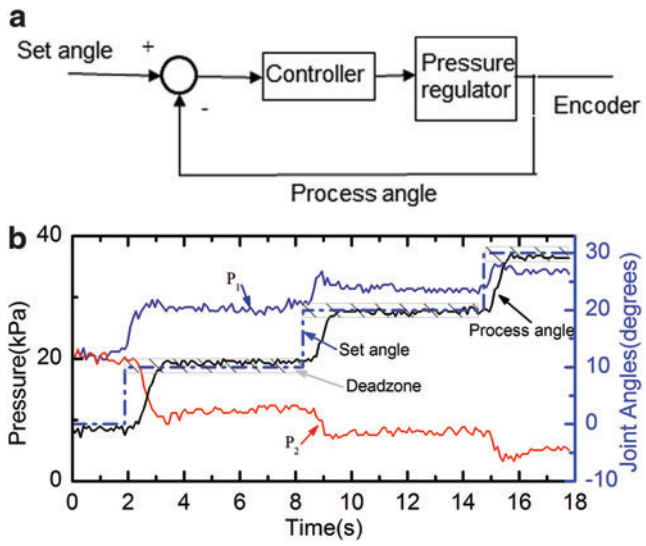

FIG. 9. Joint angle control. **(a)** Controller block diagram. **(b)** Dynamic response. Motion demonstration of the robotic joint is shown in Supplementary Video S1. Color images are available online at www.liebertpub.com/soro

According to the static models Equation (34), σ is correlated to ΔP and P_0. For a given P_0, joint angle is regulated by controlling the input pressure P_{in}, with

$$\begin{cases} P_{in} = \mathrm{P}_r, \left|\sigma_{ref} - \sigma\right| \le d \\ P_{in} = K_P(\sigma_{ref} - \sigma) + P_r, \left|\sigma_{ref} - \sigma\right| > d \end{cases}, \tag{37}$$

where P_r is the pressure read by pressure sensor, σ_{ref} is the set angle, σ is the process angle read by the rotary encoder, d is a dead-zone introduced to minimize oscillations near the target value, and K_P is the proportional control gain. Both d and K_P values were determined heuristically. The input to the two regulators is, respectively, $P_1 = P_{in}$, $P_2 = 2P_0 - P_{in}$ according to Equation (33). The controller block diagram is presented in Figure 9(a).

In this experiment, for a given series of target positions (0°, 10°, 20°, and 30°), the corresponding pressures and joint angles with time varying are shown in Figure 9(b). The robotic joint could achieve good reliability and accuracy actuated by FORAs. After a new desired angle was set, the pressure took around 0.1 s to respond, and the pressure signal settles after around 1 s. As a result, the joint also took around 0.1 s to respond and took an average of 1.7 s to settle. The time delay mainly comes from the pressure regulation. Methods on achieving faster response to improve the speed of pressure regulation will be investigated in the future.

Conclusion and Future Work

In this article, a novel soft linear actuator was proposed with improved performances over the popular McKibben-type PAMs, offering nearly doubled motion range, substantially improved force profile, and significantly lower actuation pressure. The desirable feature set of the new FORA was made possible by the newly proposed origamic chamber that generated radial expansion under pressure while contracting axially. Combining this new origamic chamber with an external fiber mesh, the FORA could generate very high traction force (over 150N) and very large contractile motion (over 50%) at very low input pressure (100 kPa).

Moreover, thanks to the origamic structure which kept the input pressure for chamber expansion to a minimal level, we could derive elegant analytical models to describe the quasi-static behaviors of FORA at a reasonable accuracy and even use the models to predict force outputs. The origamic chamber design was also characterized thoroughly to provide guidelines on how to design a chamber to achieve the desired FORA performance.

Fabrication of the FORA was mainly facilitated by 3D printing to achieve high customizability with very good repeatability and low cost. We have provided a detailed list of material selection and dimension considerations for a quick start on designing and fabricating FORAs for any desired performance specifications.

To thoroughly evaluate the performances of FORA actuator, we developed a dedicated soft-actuator testing platform and provided a detailed list of components. The fabricated FORAs following the proposed fabrication procedures were tested using the platform and compared against commercially available PAMs of similar dimensions, and the FORA had shown highly superior performances. The analytical motion and force models for FORA were also compared against experimental results with very good agreements.

Finally, to showcase the benefits of FORA performance improvements on real robotic applications, we have developed a robotic joint driven by two FORAs antagonistically. It was shown both in modeling and experiments that the large motion range and high output force from FORA could contribute to both a larger motion range (120°) and high torque (>8 Nm) at very low pressure (100 kPa) with a very compact size (260 mm).

With its simple structure, highly characterized mechanism, easy fabrication procedure, and very desirable performance, FORA could easily be customized according to application requirements and fabricated in any laboratory with access to a 3D printer and used in soft robotic applications. With the substantially improved performance set of FORA, robotic design using soft actuators could be released from the PAM performance constrains. This will pave the way to the wider adaptation and application of soft robotic systems.

In future works, we will explore new methods to reduce friction and miniaturize the actuator. The dynamic characteristics of FORA will also be investigated more thoroughly. A new control approach tailored to the nonlinear nature and the pneumatic actuation of FORA will be formulated to improve the dynamic performance. In addition, the efficiency of the whole system will also be investigated.

Acknowledgments

The presented research is supported partially by Hong Kong RGC-ECS Grant 27210315, HKU Seed Funding for Basic Research 201511159051 and 201611159196.

Author Disclosure Statement

Z.W. and J.Y. are inventors on a patent No. 201621354421.5 submitted by HKU. The remaining authors declare that they have no competing interests.

References

1. Rus D, Tolley MT. Design, fabrication and control of soft robots. Nature 2015;521:467–475.
2. Kim S, Laschi C, Trimmer B. Soft robotics: a bioinspired evolution in robotics. Trends Biotechnol 2013;31:287–294.
3. Wang Z, Chen MZ, Yi J. Soft robotics for engineers. HKIE Trans 2015;22:88–97.
4. Holland DP, Abah C, Velasco-Enriquez M, *et al.* The Soft Robotics Toolkit: strategies for Overcoming Obstacles to the Wide Dissemination of Soft-Robotic Hardware. IEEE Robot Autom Mag 2017;24:57–64.
5. Wang Z, Peer A, Buss M. An HMM approach to realistic haptic human-robot interaction. In: EuroHaptics conference, 2009 and Symposium on Haptic Interfaces for Virtual Environment and Teleoperator Systems. World Haptics 2009. Third Joint, Salt Lake City, UT, March 18, 2009, pp. 374–379.
6. Wang Z, Sun Z, Phee SJ. Haptic feedback and control of a flexible surgical endoscopic robot. Comput Methods Programs Biomed 2013;112:260–271.
7. Shepherd RF, Ilievski F, Choi W, *et al.* Multigait soft robot. Proc Natl Acad Sci 2011;108:20400–20403.
8. Polygerinos P, Wang Z, Overvelde JT, *et al.* Modeling of soft fiber-reinforced bending actuators. IEEE Trans Robot 2015;31:778–789.
9. Wang Z, Polygerinos P, Overvelde JT, Galloway KC, Bertoldi K, Walsh CJ. Interaction forces of soft fiber reinforced bending actuators. IEEE/ASME Trans Mechatronics 2017;22:717–727.
10. Galloway KC, Becker KP, Phillips B, *et al.* Soft robotic grippers for biological sampling on deep reefs. Soft Robot 2016;3:23–33.
11. Chen FJ, Dirven S, Xu WL, Li XN. Soft actuator mimicking human esophageal peristalsis for a swallowing robot. IEEE/ASME Trans Mechatronics 2014;19:1300–1308.
12. Kode VR, Cavusoglu MC. Design and characterization of a novel hybrid actuator using shape memory alloy and dc micromotor for minimally invasive surgery applications. IEEE/ASME Trans Mechatronics 2007;12:455–464.
13. Carpi F, Salaris C, De Rossi D. Folded dielectric elastomer actuators. Smart Mater Struct 2007;16:S300.
14. Choi HR, Jung K, Ryew S, *et al.* Biomimetic soft actuator: design, modeling, control, and applications. IEEE/ASME Trans Mechatronics 2005;10:581–593.
15. Polygerinos P, Wang Z, Galloway KC, Wood RJ, Walsh CJ. Soft robotic glove for combined assistance and at-home rehabilitation. Robot Autonom Syst 2015;73:135–143.
16. Miron G, Plante JS. Design principles for improved fatigue life of high-strain pneumatic artificial muscles. Soft Robot 2016;3:177–185.
17. Tondu B. Modelling of the McKibben artificial muscle: a review. J Intell Mater Syst Struct 2012;23:225–253.
18. Chou CP, Hannaford B. Measurement and modeling of McKibben pneumatic artificial muscles. IEEE Trans Robot Autom 1996;12:90–102.
19. Tsagarakis N, Caldwell DG. Improved modelling and assessment of pneumatic muscle actuators. In: Robotics and Automation, 2000. Proceedings. ICRA'00. IEEE International Conference on 2000, Vol. 4, pp. 3641–3646.
20. Wang G, Wereley NM, Pillsbury T. Non-linear quasi-static model of pneumatic artificial muscle actuators. J Intell Mater Syst Struct 2015;26:541–553.
21. Yi J, Shen Z, Song C, Wang Z. A soft robotic glove for hand motion assistance. In: Real-time Computing and Robotics (RCAR), IEEE International Conference on Jun 6, 2016, pp. 111–116.
22. Festo Company, Germany. Fluidic muscle. www.festo.com (accessed March 2016).

23. Shadow Robot Group, UK. The shadow air muscle. www.shadow.org.uk (accessed March 2016).
24. Parker Company, USA. Cylinder. www.parker.com (accessed September 2016).
25. Daerden F, Lefeber D, Verrelst B, Van Ham R. Pleated pneumatic artificial muscles: actuators for automation and robotics. In: Advanced Intelligent Mechatronics, 2001. Proceedings, 2001 IEEE/ASME International Conference on 2001, Vol. 2, pp. 738–743.
26. Martinez RV, Fish CR, Chen X, Whitesides GM. Elastomeric origami: programmable paper-elastomer composites as pneumatic actuators. Adv Funct Mater 2012;22:1376–1384.
27. Onal CD, Wood RJ, Rus D. An origami-inspired approach to worm robots. IEEE/ASME Trans Mechatronics 2013;18:430–438.
28. Kobayashi H, Kresling B, Vincent JF. The geometry of unfolding tree leaves. Proc R Soc Lond B Biol Sci 1998;265: 147–154.
29. Liu S, Lu G, Chen Y, Leong YW. Deformation of the Miura-ori patterned sheet. Int J Mech Sci 2015;99:130–142.
30. Popov VL. Contact Mechanics and Friction. Berlin: Springer Berlin Heidelberg, 2010.
31. Roff WJ, Scott JR. Fibres, Films, Plastics and Rubbers: A Handbook of Common Polymers. London: Elsevier, 2013.
32. Tondu B, Ippolito S, Guiochet J, Daidie A. A seven-degrees-of-freedom robot-arm driven by pneumatic artificial muscles for humanoid robots. Int J Robot Res 2005;24:257–274.
33. Caldwell DG, Medrano-Cerda GA, Bowler CJ. Investigation of bipedal robot locomotion using pneumatic muscle actuators. In: Robotics and Automation, 1997. Proceedings, 1997 IEEE International Conference on, April 20 1997, Vol. 1, pp. 799–804.
34. Schroder J, Erol D, Kawamura K, Dillman R. Dynamic pneumatic actuator model for a model-based torque controller. In: Computational Intelligence in Robotics and Automation, 2003. Proceedings, 2003 IEEE International Symposium on, July 16, 2003, Vol. 1, pp. 342–347.

Address correspondence to:
Zheng Wang
Department of Mechanical Engineering
The University of Hong Kong
719 Haking Wong Building
Pokfulam, Hong Kong 999077
China

E-mail: zheng.wang@ieee.org